PHYSICAL REVIEW MATERIALS **4**, 083404 (2020)

Incorporating density jumps and species-conserving dynamics in XPFC binary alloys

Matthew J. Frick
Department of Physics, Centre for the Physics of Materials, McGill University, Montreal, Quebec H3A 2T8, Canada

Nana Ofori-Opoku
Computational Techniques Branch, Canadian Nuclear Laboratories, Chalk River, Ontario K0J 1J0, Canada

Nikolas Provatas
Department of Physics, Centre for the Physics of Materials, McGill University, Montreal, Quebec H3A 2T8, Canada

(Received 20 May 2020; accepted 28 July 2020; published 27 August 2020)

This work presents a consistent formulation of the structural phase-field-crystal model of substitutional binary alloys that allows for the description of phases of unequal densities, a key feature in solidification. We further develop the dynamics of the model to be consistent with conserved Langevin dynamics in the true governing species densities. Additionally, this work expands on the ability to control pressure, so far only implemented in pure materials, to binary alloys by improving the control system that controls pressure from previous work. We study the equilibrium properties of the new model and demonstrate that control of pressure can drive various kinematic microscopic processes in materials such as grain boundary premelting, phase instability, and grain or interphase boundary motion.

DOI: 10.1103/PhysRevMaterials.4.083404

I. INTRODUCTION

The macroscopic material properties of engineering alloys have long been understood to arise out of a complicated relationship to the microstructure that forms during the casting and thermomechanical processing of a material. However, due to the prohibitive difficulty of directly imaging or performing *in situ* measurements during these processes the understanding of the microstructural formation is often empirical.

Advances in the ability to predict microstructure have been largely driven by atomistic and mesoscale phase field type modeling. One such class of models are so-called phase field crystal (PFC) models [1]. These are phase field models with a periodic order parameter, which allow the resolution of atomic-scale structure and defects that evolve on inherently diffusive timescales. This class of models thus has many of the complex physical mechanism that need to be built into traditional phase field models such as strain relaxation, elasticity, and arbitrary grain orientation; these arise holistically from the form of a PFC free energy [2]. The ability to model robust types of crystal structures beyond that possible in the original PFC model has since led to a class of PFC models referred to as structural phase field crystal (XPFC) models [3–5], the alloy version of which was then expanded upon to model arbitrary enthalpy of mixing by Smith *et al.* [6].

A key feature absent from past PFC models has been a consistent description and control of bulk density or volume changes between phases. This is a crucial prerequisite required of any model describing shrinkage and void formation during rapid solidification, as well as free surface creation under stress. This problem was first addressed in pure materials by Schwalbach *et al.* [7] using a phenomenological interpolation function between gaseous and condensed phases. Kocher *et al.* [8] recently formulated a more complete analysis of vapor in pure materials by expanding in a single field about a fluid capable of taking on both gaseous and condensed forms and introducing pressure to consider coexistence in pure materials in density(ρ)-pressure(p)-temperature(T) space. The first step toward controlling the ρ-p-T space of a vapor forming binary alloy has been attempted by Wang *et al.* [9] using a phenomenology that interpolates the free energy of a simple triangular-forming crystal phase with a liquid-vapor system through changes in local bulk density. The dynamics of this vapor-forming PFC model, like all previous alloy PFC models, suffers from the fact that density and concentration evolve as separate conserved fields. These dynamics are incorrect when large bulk density changes are allowed, which is the case in solidification processes.

In this paper we address the issue of consistently describing the density-pressure-temperature-concentration (ρ-p-T-c) space of complex binary alloys and their dynamics in the paradigm of the the XPFC alloy model of Smith *et al.* [6]. We begin by reinterpreting the fields of the XPFC free energy. We then generalize some of the ideas of Kocher *et al.* [8] to control density-pressure-temperature-concentration space of a binary system that can form different crystal phases. Moreover, by connecting solute concentration (c) and total density (ρ) to the individual species densities of a binary system ρ_A, ρ_B, we introduce alloy dynamics for total density ρ and concentration c that is consistent with the conservation of individual species densities.

The remainder of the paper is organized as follows. Section II reviews the derivation of the original XPFC alloy model of Greenwood *et al.* [5], highlighting recent

©2020 American Physical Society

improvements regarding the enthalpy of mixing. In Sec. III, we reintroduce the definition of concentration (c) in the XPFC alloy model such as to be consistent with the notion of a smooth c field that is coupled to a microscopic density. The dynamics of the alloy XPFC model are then reformulated in terms of individual species densities of the binary alloy. This section also introduces algorithms for implementing pressure and volume changes during dynamical simulations. Section IV then studies the equilibrium properties of the reformulated XPFC alloy model in density(ρ)-pressure(p)-concentration(c)-temperature(T) space. The demonstration of the model in effecting pressure controlled kinematics is shown in Sec. V, while the application of the model to solute drag is located in Sec. VI. We conclude in Sec. VII.

II. XPFC MODEL OF BINARY ALLOYS

The binary XPFC alloy model has been established for several years as a PFC phenomenology for simulating substitutional binary alloys that crystallize into a wide range of crystalline symmetries [1,10–19]. As with any PFC theory, it can be derived from classical density-functional theory of mixtures [20], where the density fields of the two components ρ_A and ρ_B are transformed according to the following relations

$$\begin{aligned} n &= \frac{\rho_A + \rho_B - \rho_0}{\rho_0} \\ c &= \frac{\rho_B}{\rho_A + \rho_B}, \end{aligned} \tag{1}$$

where n is the total dimensionless density, c is the concentration of the B component, and $\rho_0 = \rho_A^0 + \rho_B^0$ is the total reference density around which the theory is nominally expanded. A key assumption of the XPFC alloy theory is to assume that the c field is locally smooth compared to n in order to arrive at the XPFC free energy. This makes it possible to couple the microscopic density field n to only the long wavelength properties of concentration c, as tacitly reflected in the form of the XPFC alloy model reviewed below.

With the variable transforms and assumptions stated above, the free energy functional for an XPFC binary alloy becomes

$$\begin{aligned} \frac{\Delta F}{\rho_0 k_B T} = \int d^3r \bigg\{ &\frac{n}{2}(1 - C_{nn}*)n - \frac{t}{6}n^3 + \frac{v}{12}n^4 \\ &+ w(n+1)S_{\text{mix}} - \frac{1}{2} c\, C_{cc} * c \bigg\}, \end{aligned} \tag{2}$$

where we have introduced the notation $A * B$ to represent a convolution operation, while t, v, and w are phenomenological fitting parameters, and S_{mix} is the entropy of mixing, given by

$$S_{\text{mix}} = c \ln\left(\frac{c}{c_0}\right) + (1-c)\ln\left(\frac{1-c}{1-c_0}\right), \tag{3}$$

where c_0 is a reference concentration ρ_B^0/ρ_0. Ordering in the total mass density is controlled through the direct correlation function C_{nn}, which has the form

$$C_{nn}(|r - r'|) = \sum_{i \in \mathcal{N}} \xi_i(c) C_i(|r - r'|), \tag{4}$$

where $\mathcal{N}$ sums over an arbitrary number of ordered phases possible and C_i encodes for the density ordering of the phase i. Equation (4) allows for changes in crystal structure between phases by coupling each C_i to the local composition c, via the functions $\xi_i(c)$. One such interpolation function for eutectic alloys was proposed by Greenwood *et al.* [5] as

$$\begin{aligned} \xi_A(c) &= 1 - 3c^2 + 2c^3, \\ \xi_B(c) &= \xi_A(1-c), \end{aligned} \tag{5}$$

and will be used throughout the remainder of the paper.

In XPFC models, the short wavelength properties of the correlation functions C_i are controlled in Fourier space by superimposing a series of Gaussian peaks of the form

$$C_i(k) = e^{-\frac{T}{T_M}} \max(\{G_j(k)\}), \tag{6}$$

where T_M is the melting temperature [19], the $\max(\cdots)$ function denotes taking the maximal value from the set of its arguments, and the arguments are made up by a set of Gaussians,

$$G_j(k) = e^{-\frac{(k-k_j)^2}{2\sigma_j^2}}, \tag{7}$$

where $k_j = 2\pi/\lambda_j$ where λ_j is the wavelength of the given crystallographic plane, and σ_j is the width of the Gaussian, which is related to the elasticity of the crystal. To the sum of Eq. (6) can also be added a negative $k = 0$ peak that can further be used to control the compressibility of emerging solid phases.

In the model of Eq. (2), correlations in concentration fluctuations are controlled through $C_{cc}(|r - r'|)$. In the long-wavelength limit, Smith *et al.* [6] proposed a form for C_{cc} given by

$$C_{cc}(r - r') = -w\epsilon(T)\delta(r - r') - W_c \nabla^2 \delta(r - r'). \tag{8}$$

Applying the divergence theorem, under suitable boundary conditions, to the C_{cc} term in Eq. (2) yields a more familiar form of the XPFC binary alloy free energy functional,

$$\begin{aligned} \frac{\Delta F}{\rho_0 k_B T} = \int d^3r \bigg\{ &\frac{n}{2}(1 - C_{nn}*)n - \frac{t}{6}n^3 + \frac{v}{12}n^4 \\ &+ w(n+1)S_{\text{mix}} + \frac{1}{2}W_c|\nabla c|^2 \\ &+ \frac{1}{2}w\epsilon(T)(c - c_0)^2 \bigg\}. \end{aligned} \tag{9}$$

Equation (9) contains energy penalties for concentration gradients as prescribed by Cahn and Hilliard [21], as well as the leading order enthalpy of mixing contribution.

III. IMPROVEMENTS TO THE CONSISTENCY OF THE XPFC ALLOY MODEL

The free energy as derived in Sec. II, and its dynamics, have been shown to qualitatively reproduce a host of physical phenomena [1,10–19]. The model has been especially convenient for calculating equilibrium properties of systems, since n and c are the natural variables used in physical metallurgy. However, when considering dynamical processes, particularly those accompanied by significant density changes, difficulties arise from the use of these variables due to the fact c is not truly a conserved field and as such is not governed by conserved Langevin dynamics. Strictly speaking, the conserved variables of our system are ρ_A and ρ_B. Another problem with the XPFC alloy model is that it tacitly assumes that the concentration c field is smooth, although small spatial oscillations do in fact develop in it in some processes. These issues are both addressed next.

A. Redefining XPFC concentration

In order to derive dynamics for this system in the governing density variables of ρ_A and ρ_B of components A and B, respectively, we revisit the underlying assumption made in the original derivation of Greenwood *et al.* [5]. Therein, a critical explicit assumption was the smoothness of the c field, which implies the substitutional nature of the alloy model. In doing so, it allowed the simplification of convolution integrals involving c. These assumptions, and consequent manipulations of the free energy ensured the impossibility of a return to a ρ_A–ρ_B formulation due to the information lost in this smoothing process. To rectify this, while maintaining a connection with the variables c and n, we consider the relationship that already exists between n and c and ρ_A and ρ_B. Namely, we insist on the smoothness of the concentration field by positing a relationship of the form

$$c \equiv \frac{\chi * \rho_B}{\chi * (\rho_A + \rho_B)}, \tag{10}$$

where χ is a smoothing kernel that retains long wavelength information of the field upon which it operates. This is similar to the use of smoothing kernels employed by Kocher *et al.* [8] and is defined in reciprocal space as

$$\tilde{\chi}(k) \equiv e^{-\frac{k^2}{2\lambda_c}}, \tag{11}$$

where λ_c sets the cutoff wavelength. Moreover, this definition of c also recovers the equilibrium definition of concentration as a bulk quantity.

We make the further improvement of scaling the free energy by a reference temperature instead of the model temperature, as was done by Kocher *et al.* [8]. This introduces a factor of reduced temperature $\tau = T/T_0$ in the free energy functional, according to

$$\begin{aligned}\frac{F}{\rho_0 k_\mathrm{B} T_0} = \tau \int d^3r \bigg\{ &\frac{n}{2}(1 - C_{nn}*)n - \frac{t}{6}n^3 + \frac{v}{12}n^4 \\ &+ w(n+1)S_\mathrm{mix} + \frac{1}{2}w\epsilon(T)(c - c_0)^2 \\ &+ \frac{1}{2}W_c|\nabla c|^2 \bigg\} + \tau \bar{F}(\rho_0, c_0),\end{aligned} \tag{12}$$

where Eq. (12) also retains the free energy of the reference fluid, $\bar{F}(\rho_0, c_0)$. This term will be largely neglected throughout this paper as it will not affect either the phase diagram or the dynamics; its primary importance is in quantifying the reference pressure of our system.

B. Density field dynamics

With the reformulation of the concentration introduced in Sec. III A, the dynamical evolution of the alloy system may be calculated with respect to its governing variables ρ_A and ρ_B. Namely, conserved dynamics in these fields follow

$$\frac{\partial \rho_i}{\partial t} = \nabla \cdot (M_i \nabla \mu_i) \approx M_i \nabla^2 \left(\frac{\delta F}{\delta \rho_i} \right), \tag{13}$$

where M_i is the mobility of the constituent density, assumed for simplicity to be a constant here, and μ_i is the chemical potential of the constituent. The chemical potential is calculated from the (n, c)-based free energy by means of the functional chain rule

$$\begin{aligned}\frac{\delta F[n,c](r')}{\delta \rho_i(r)} = \int d^3r'' \bigg[&\frac{\delta n(r'')}{\delta \rho_i(r)} \frac{\delta F[n,c](r')}{\delta n(r'')} \\ &+ \frac{\delta c(r'')}{\delta \rho_i(r)} \frac{\delta F[n,c](r')}{\delta c(r'')} \bigg].\end{aligned} \tag{14}$$

Application of this chain rule gives the respective chemical potentials of each species as

$$\begin{aligned}\frac{\mu_A}{\rho_0 k_\mathrm{B} T_0} =& \tau \left\{ (1 - C_{nn}) * n(r) - \frac{t}{2}n^2(r) + \frac{v}{3}n^3(r) + w\left(c(r) \ln\left(\frac{c(r)}{c_0}\right) + (1 - c(r)) \ln\left(\frac{1 - c(r)}{1 - c_0}\right) \right) \right\} \\ &- \tau \int d^3r'' \chi(r'' - r) \frac{c(r'')}{\int d^3r''' \chi(r''' - r'')(n(r''') + 1)} \times \left[w(n(r'') + 1)\left(\ln\left(\frac{c(r'')}{c_0}\right) - \ln\left(\frac{1 - c(r'')}{1 - c_0}\right) \right) \right. \\ &\left. + w\epsilon(T)(c(r'') - c_0) - W_c \nabla^2 c(r'') \right] \\ &+ \frac{\tau}{2} \int d^3r'' \chi(r'' - r) \frac{c(r'')}{\int d^3r''' \chi(r''' - r'')(n(r''') + 1)} n(r'') \int d^3r' n(r') \frac{\partial C_{nn}(r', r'')}{\partial c},\end{aligned} \tag{15}$$

$$\begin{aligned}\frac{\mu_B}{\rho_0 k_\mathrm{B} T_0} =& \tau \left\{ (1 - C_{nn}) * n(r) - \frac{t}{2}n^2(r) + \frac{v}{3}n^3(r) + w\left(c(r) \ln\left(\frac{c(r)}{c_0}\right) + (1 - c(r)) \ln\left(\frac{1 - c(r)}{1 - c_0}\right) \right) \right\} \\ &+ \tau \int d^3r'' \chi(r'' - r) \frac{1 - c(r'')}{\int d^3r''' \chi(r''' - r'')(n(r''') + 1)} \times \left[w(n(r'') + 1)\left(\ln\left(\frac{c(r'')}{c_0}\right) - \ln\left(\frac{1 - c(r'')}{1 - c_0}\right) \right) \right. \\ &\left. + w\epsilon(T)(c(r'') - c_0) - W_c \nabla^2 c(r'') \right] \\ &- \frac{\tau}{2} \int d^3r'' \chi(r'' - r) \frac{1 - c(r'')}{\int d^3r''' \chi(r''' - r'')(n(r''') + 1)} n(r'') \int d^3r' n(r') \frac{\partial C_{nn}(r', r'')}{\partial c}.\end{aligned} \tag{16}$$

We draw particular attention here to the terms premultiplying the inter-diffusion potential $\mu_{\text{inter}} = \delta F/\delta c$, which demonstrate why Eq. (10) must be written with smoothing kernels in both the numerator and denominator. If a single smoothing kernel is used which acts on the traditional definition of the concentration, this prefactor will have a term which goes as $1/(n(r)+1)$ which can result in numerical instabilities due to the oscillations in the n field.

Due to the critical role of the smoothing kernels in the evaluation of Eqs. (15) and (16), the FFTW algorithm [22] is used to allow for efficient calculation of convolutions. We thus choose to utilize the semi-implicit spectral Fourier method [23, App. A.4] in the numerical implementation of the conserved dynamics in Eq. (13).

C. Dynamical pressure control and volume dynamics

To describe pressure changes during dynamical simulations, we follow the work of Kocher *et al.* [8] and utilize the grand potential density as an approximation for system pressure, thus allowing for isobaric or pressure controlled systems. The grand potential density is defined as

$$\omega = \frac{1}{V}\int_V d^3r\left(f - \sum_i \mu_i\rho_i\right), \tag{17}$$

where f is the free energy density of the multicomponent alloy. Specializing to a binary alloy, the grand potential density can now be calculated using Eqs. (12), (15), and (16). Generalization to a multicomponent alloy is straightforward.

For single component systems Ref. [8] used a two step process. The first step is a mass conserving flux of the form

$$J_n = -n_0(t) + n_0(t_0)\left(\frac{\Delta x(t_0)}{\Delta x(t)}\right)^d, \tag{18}$$

where Δx is the side length of the volume element, which is assumed to be a d cube where d is the dimensionality of the system, t is the simulation time, t_0 is the initial time, and n_0 is the global average density of the system. This flux is added to each volume element. The second step is changing the volume element with a proportional feedback loop defined as

$$\Delta x(t) = \Delta x(t-\Delta t) + \frac{\Delta t M_p}{d(\Delta x)^{d-1}}(\omega - P_0), \tag{19}$$

where P_0 is the target pressure, Δt is the length of a numerical time step, and M_p is the mobility parameter for readjustments to the volume element—i.e., the ability of the system to respond to pressure differentials. This feedback loop is applied after each time step of the governing equations.

While such a density flux and feedback loop conserves the total mass of the system, it violates the physics of diffusion transport. Under a compression of a volume element, a low density element and a high density element both receive the same density flux into the system. Local mass is thus not conserved as the low density volume element has gained a larger fraction of its density than the high density element; mass has effectively moved instantaneously from the high density region to the low density region. We illustrate a one-dimensional example of this phenomenon in Fig. 1(a), and the correction using the scheme that we implement in this work (discussed below) to remedy this problem in Fig. 1(b).

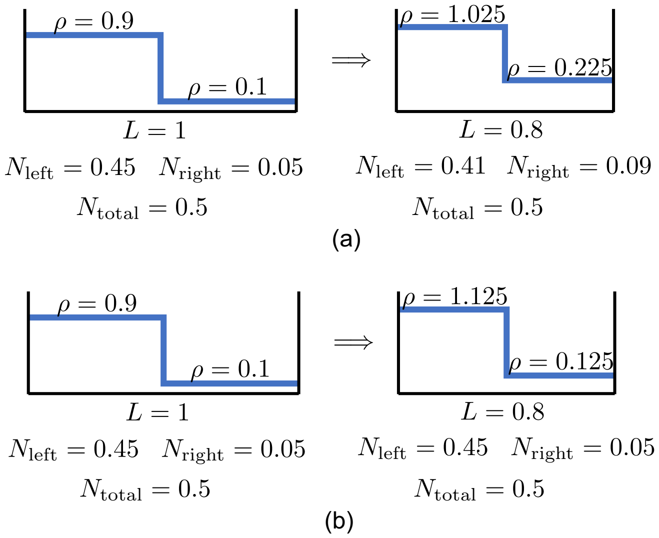

FIG. 1. A two phase system undergoing a number conserving change in volume as described by (a) Eqs. (18) and (19) and (b) Eqs. (24) and (25).

To maintain consistent diffusion behavior we propose a slightly different mass conserving step. Local conservation of total number (N), or mass, requires that

$$\frac{\partial N}{\partial t} = \frac{\partial(\bar{\rho}V)}{\partial t} = 0\,, \tag{20}$$

where V is the volume and $\bar{\rho}$ is the average density of the system or subsystem. After expressing the volume as a numerical grid, $V = \Pi_{i=1}^{d}\Delta x N_i$, and combining with the volume feedback loop proposed by Kocher *et al.*,

$$\frac{\partial\,\Delta x}{\partial t} = \frac{M_p}{d\,(\Delta x)^{d-1}}(\omega - P_0)\,, \tag{21}$$

Eq. (20) can be rewritten as

$$\frac{\partial\bar{\rho}}{\partial t} = -\frac{M_p(\omega - P_0)}{(\Delta x)^d}\bar{\rho}\,. \tag{22}$$

In pursuit of a closed form solution for the numerical update scheme of Eq. (22), we posit that this equation can be solved via separation of variables and integration,

$$\int\frac{d\bar{\rho}}{\bar{\rho}} = \int dt\,\frac{M_p(\omega - P_0)}{(\Delta x)^d}\,, \tag{23}$$

which leads to the numerically approximated solution

$$\bar{\rho}(x, t+\Delta t) = \bar{\rho}(x,t)e^{-\frac{M_p(\omega - P_0)\Delta t}{(\Delta x)^d}}\,. \tag{24}$$

After a point-wise evaluation of this local density adjustment on each grid element, we then ensure total conservation of mass by appropriately updating Δx. This update leads to a revision of Δx of the form

$$J_{\Delta x} = -\Delta x(t) + \Delta x(t_0)\left(\frac{\int_{V_{\text{total}}} d^d r\rho(t)}{\int_{V_{\text{total}}} d^d r\rho(t_0)}\right)^{1/d}, \tag{25}$$

where Eq. (25) is iterated until $J_{\Delta x}$ reaches zero. Due to the numerical constraints of the FFTW [22] library used in our dynamics, the volume element must be a constant throughout the simulation domain. Thus, we must apply Eq. (25) to each volume element individually in such a way that the global update of [common] volume element size conserves mass in local subdomains of volume elements in the system. As any arbitrary subdomain of the system must conserve its own local mass we choose to update the smallest possible subdomain—i.e., each pixel—as it is both numerically simplest and ensures that any larger subdomain will also be conserved.

Due to the exponential nature of Eq. (24), it is imperative that the argument of the exponential remain reasonably small. To ensure this smallness, we utilize a "guess-check-correct" algorithm. For the sake of clarity we detail below the algorithmic structure of the volume dynamics, including the guess-check-correct algorithm. The steps are as follows:

(1) Set the target pressure P_0.

(2) Calculate the universal system pressure through the grand potential ω. Calculate the error $err = \omega - P_0$.

(3) Calculate a quick guess for the change in universal volume element using Eq. (19).

(4) Check if this quick guess is larger than a cutoff value.

True: Scale the time step such that Eq. (19) will give a value below the cutoff.

False: Set $\Delta t = \Delta t_{\max}$.

(5) The mean field density of each volume element is updated using Eq. (24).

(6) Conservation of the total number of particles in the entire system is enforced by calculating and applying Eq. (25) until Eq. (25) gives an output of less than a cutoff value.

This algorithm is also displayed as a pseudocode flowchart in Fig. 2.

IV. EQUILIBRIUM PROPERTIES OF MODEL

The equilibrium properties of a binary alloy, where density variations are considered, are defined in terms of the Helmholtz free energy densities by the system of Eqs. [24,25].

$$\begin{aligned}
\frac{1}{\rho_S}\frac{\partial f_S(c_S,\rho_S)}{\partial c_S} &= \mu^{\mathrm{eq}}\,,\\
\frac{1}{\rho_L}\frac{\partial f_L(c_L,\rho_L)}{\partial c_L} &= \mu^{\mathrm{eq}}\,,\\
\rho_S\frac{\partial f_S(c_S,\rho_S)}{\partial \rho_S} - f_S(c_S,\rho_S) &= p\,, \qquad (26)\\
\rho_L\frac{\partial f_L(c_L,\rho_L)}{\partial \rho_L} - f_L(c_L,\rho_L) &= p\,,\\
\frac{f_L(c_L,\rho_L)}{\rho_L} - \frac{f_S(c_S,\rho_S)}{\rho_S} &= (c_L-c_S)\mu^{\mathrm{eq}} - \left(\frac{1}{\rho_L}-\frac{1}{\rho_S}\right)p\,,
\end{aligned}$$

where we have used the short form notation f_S, ρ_S, and c_S to, respectively, denote the free energy density, total density, and concentration of the solid phase. Similarly f_L, ρ_L, and c_L, respectively, denote the free energy density, total density, and concentration of the liquid phase. Here, μ is the chemical potential and p the pressure.

The solution to the above system of equations in terms of the free energy defined in Sec. II is highly nontrivial [25]. However, the system of equations can be significantly simplified by a change of variables such that

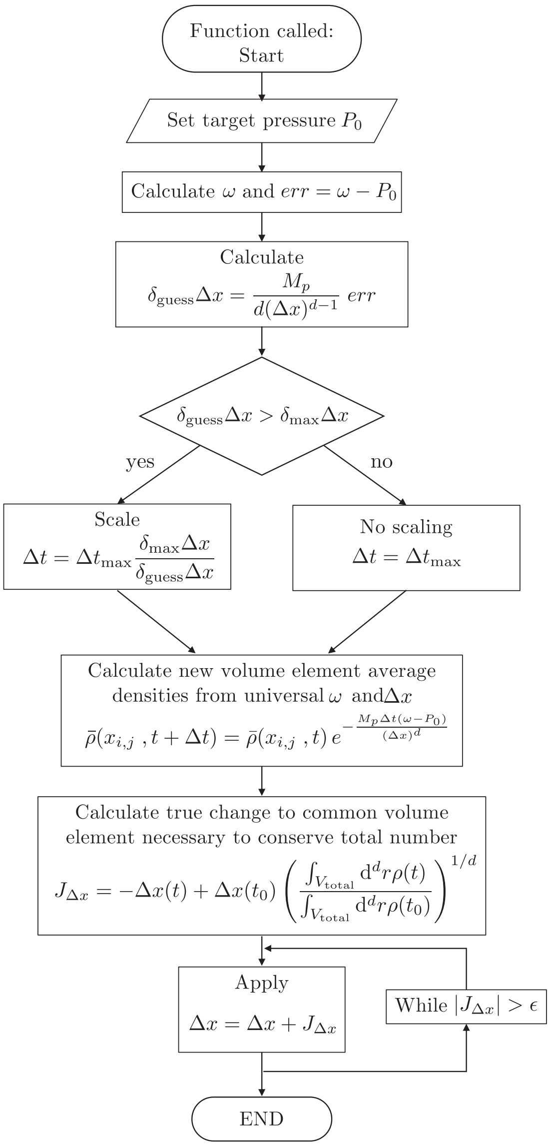

FIG. 2. Flowchart of algorithm to update the common volume element and the density in each volume element consistent with the physics of local mass conservation.

$$\mathcal{F} = \nu f\ , \qquad (27)$$

where $\nu = 1/\rho$ is the particle volume, akin to a molar volume. We note that under this transformation, the free energy density with units of J/m^3 becomes free energy per particle with units of J/particle; when multiplied by Avagadro's number, the latter becomes the standard measure used in metallurgical literature. The equilibrium equations then reduce to

$$\begin{aligned}
\frac{\partial \mathcal{F}_S(c_S,\nu_S)}{\partial c_S} &= \mu^{\mathrm{eq}}\\
\frac{\partial \mathcal{F}_L(c_L,\nu_L)}{\partial c_L} &= \mu^{\mathrm{eq}}\\
\frac{\partial \mathcal{F}_S(c_S,\nu_S)}{\partial \nu_S} &= -p \qquad (28)
\end{aligned}$$

$$\frac{\partial \mathcal{F}_L(c_L, \nu_L)}{\partial \nu_L} = -p$$
$$\mathcal{F}_L(c_L, \nu_L) - \mathcal{F}_S(c_S, \nu_S) = (c_L - c_S)\mu^{\text{eq}} - (\nu_L - \nu_S)p.$$

Equation (28) defines the equations of a common tangent plane in (ν-c-T) space. In the traditional formulations of binary PFC models—with the exception of one amplitude model [25]—the density (particle volume) are assumed to be constant across the different phases in equilibrium, which reduces Eq. (28) to

$$\frac{\partial f_S(c_S, \rho)}{\partial c_S} = \mu^{\text{eq}},$$
$$\frac{\partial f_L(c_L, \rho)}{\partial c_L} = \mu^{\text{eq}},$$
$$f_L(c_L, \rho) - f_S(c_S, \rho) = (c_L - c_S)\mu^{\text{eq}},$$

which defines the equations of a common tangent line in (c-T) space.

We use a similar, but distinct, approach to define the isobaric phase diagram from Eq. (28) as follows: For a fixed pressure we rearrange the last of Eq. (28) to the form

$$(\mathcal{F}_L(c_L, \nu_L) + \nu_L p) - (\mathcal{F}_S(c_S, \nu_S) + \nu_S p) = (c_L - c_S)\mu^{\text{eq}}. \quad (29)$$

The first two of Eq. (28) and Eq. (29) now define a common tangent in concentration along an isobaric surface, with the isobaric constraint of said surface being enforced by the third and fourth equations of Eqs. (28).

While Eq. (28) is shown in dimensional form, an identical set of dimensionless equations can be constructed by scaling the variables similarly to Eq. (12):

$$\bar{\mathcal{F}} = \frac{\mathcal{F}}{k_B T_0} = \frac{\rho_0}{\rho}\frac{f}{\rho_0 k_B T_0} \quad (30)$$
$$\bar{\mu}^{\text{eq}} = \frac{\mu^{\text{eq}}}{k_B T_0} \quad (31)$$
$$\bar{p} = \frac{\nu_0 p}{k_B T_0} = \frac{p}{\rho_0 k_B T_0} \quad (32)$$
$$\bar{\nu} = \frac{\nu}{\nu_0} = \frac{\rho_0}{\rho} \quad (33)$$

which allows the use of scaled PFC free energies of the form of Eq. (12) to be used in the construction of phase diagrams and in the subsequent dynamics.

To determine the equilibrium phase diagram it is necessary to define a free energy curve along the isobaric surface of the free energy landscape. To do so we follow the mode expansion methodology pioneered by Kirkwood and Monroe [26] in 1941 and later refined by Yousseff and Ramakrishnan [27] and approximate the total density and total particle volume of a phase as

$$n \approx n_0 + \sum_j A_j \sum_\alpha e^{ik_{\{j,\alpha\}}\cdot r}$$
$$n_0 = \frac{1}{\bar{\nu}} - 1, \quad (34)$$

where A_j are taken as nonzero in a solid phase. The index j defines a given family of modes in a solid assumed to have the same amplitude, while $k_{\{j,\alpha\}}$ is the wave vector of the lattice plane α within the family of modes j, and r is the spatial coordinate.

Substituting the density expansion ansatz of Eq. (34) in a microscopically varying free energy density of a PFC model of Eq. (12), and integrating out short scale variations over the scale of a crystal unit cell, leads to a mesoscale free energy representation of the system of the form $F(n_0(\bar{\nu}), \{A_j\}, c)$. Moreover, we note that the derivative

$$\frac{\partial \bar{\mathcal{F}}(\bar{\nu}(n_0), \{A_j\}, c)}{\partial \bar{\nu}} \equiv \omega(\bar{\nu}(n_0), \{A_j\}, c), \quad (35)$$

where ω is the amplitude-expanded grand potential density. Thus we can enforce the pressure constraint by equating the amplitude-expanded grand potential density to the negative of the target pressure. As with all mode expansion formulations this requires a selection of crystallographic orientation; as there are no phase boundaries in a mode expansion and as PFC kernels are specifically chosen to be isotropic this choice is arbitrary.

The protocol for evaluating the equilibrium states of the alloy proceeds next as follows: For each value of the average concentration c we numerically minimize the set of amplitudes $\{n_0, A_j\}$ and primary wave-vector magnitude $k_1 = |k_{\{1,\alpha\}}|$ subject to the pressure constraint to build the isobaric free energy curve using Mathematica [28]. Only the location of the first peak of a given crystalline structure will be minimized; further peaks are placed based on their relative position to the first peak for a perfect crystal under zero strain. For the special case of a single crystalline structure a single minimization will yield the free energy values for both the solid $\{A_j\} \neq 0$ and liquid $\{A_j\} = 0$. In the more generic case of multiple crystalline structures, a minimization is required for each solid phase; the set of free energies are then compared and only the minimum is kept. This (minimum) free energy is then shifted as per Eq. (29) and passed to Mathematica's convex hull finding algorithm, which acts as a common tangent finding algorithm when passed a one-dimensional landscape. This procedure is repeated for each pressure and/or temperature of interest.

Using the conserved dynamics described by Eqs. (13) and constrained to an isobaric phase space by the algorithm outlined in Fig. 2 we validate the accuracy of the mode expansion approximation used to generate phase diagrams for the case of an eutectic alloy. Without loss of generality, we consider an alloy of structurally similar elements, differing only in the equilibrium lattice parameters of the constituent elements.

The initial conditions are set algorithmically based on a reference system to ensure that the system does not exhibit a pressure significantly different than the set target. The algorithm is as follows:

(1) The temperature, mean composition, expected phases, and initial phase composition offset relative to the mean are selected.

(2) The structure or structures are seeded into the liquid, and both phases are offset in composition in opposite directions from the mean by a small offset. For example, for an expected coexistence between the α solid and liquid, the solid would be offset by $-c_{\text{offset}}$ while the liquid would be offset by $+c_{\text{offset}}$. We found that this offset is not strictly necessary but

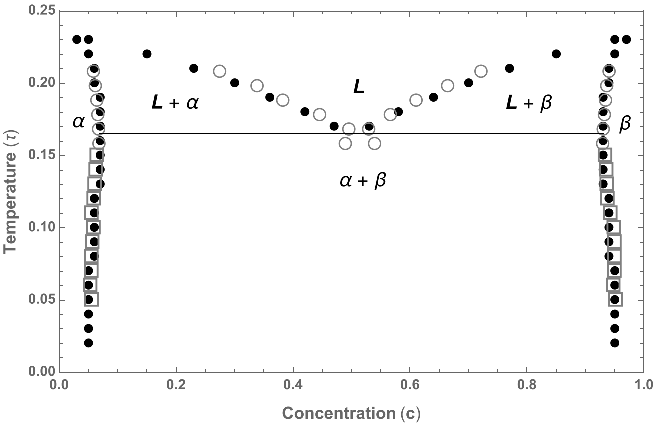

FIG. 3. Constant pressure phase diagram for a eutectic triangle-triangle system. The reduced model pressure of $P_0 = 0.01$. The parameters used in the ideal free energy were $t = 1.4$, $v = 1.0$, $w = 0.02$, $c_0 = 0.5$, and $\epsilon(T) = 0$ for simplicity. The correlation kernel of the excess free energy used parameters $k_{10}^{(A)} = 2\pi$, $\sigma_{10}^{(A)} = 0.8$, $T_M^{(A)} = 1.0$, $k_{10}^{(B)} = 7.83185307179586 \approx 2.5\pi$, $\sigma_{10}^{(B)} = 0.8$, and $T_M^{(B)} = 1.0$. The equilibrium coexistence concentrations as numerically calculated by mode expansion are shown in filled black circles while the concentrations extracted from the bulk concentrations of the dynamical simulations between liquid-solid coexistence are shown in hollow gray circles and those values extracted from dynamical simulations for solid-solid coexistence are shown in hollow gray squares.

helps to speed up the equilibration so long as the offset is in the proper direction.

(3) If a liquid-solid coexistence is selected, the solid is given a small total density increase.

(4) If a eutectic coexistence is selected then a bicrystal is seeded with a given misorientation.

(5) Equation (24) is iterated without changing the volume element until the system is suitably close to the target pressure, $|\omega - P_0| \leqslant 10^{-6}$.

Once these steps are complete, the total number of particles is calculated and will be conserved in all further iterations; this state serves as the initial condition for the simulation.

All simulations used to verify our phase diagram were performed on a 128 by 1024 pixel grid using a square volume element with initial size $\Delta x(t = 0) \approx 0.0815$ and reference temperatures of $T_0 = T_M = 1.0$. To assist with rapid equilibration, the mobilities were set to be extremely high compared to the pressure relaxation coefficient: $M_A = M_B = 20$, $M_p = 0.1$. The cutoff wavelength was set as in Kocher *et al.* [8] to be $\lambda_c = 0.21$. After equilibration of the simulation the resulting bulk concentration and bulk average total density for each phase is compared to that of the numerically approximated phase diagram. These results are shown in Fig. 3. To avoid repeated overhead in the form of initialization, wherever possible the simulations were continued and quenched by steps of $\Delta T = 0.01$ over 10 000 simulation steps. For the eutectic simulations, a misorientation of 0.1 rad ≈5.73° was used. When deep in the eutectic coexistence region, the composition profiles of a bicrystal exhibit small-amplitude long-wavelength oscillations about their equilibrium values on length scales greater than the lattice planar wavelengths. This is due to the fact that for a solid-solid system with two differing lattice constants it is not possible to create a box size commensurate to zero stress in both crystals.

V. PRESSURE CONTROLLED PHASE TRANSFORMATION KINETICS

In this section we demonstrate the ability to control various nonequilibrium phase transformations through the system pressure. Each of the following demonstrations can be achieved through quenches in temperature, however, here, we will be considering an isothermal system subjected to different pressures, compression or tension only.

In each of the following simulations we will consider a 128 × 1024 pixel grid with square volume elements with initial size $\Delta x \approx 0.0818$ and a constant reduced temperature $\tau = 0.15$, with reference temperatures of $T_0 = T_M = 1.0$. The ideal free energy fitting parameters are $t = 1.4$, $v = 1.0$, $w = 0.02$, and $c_0 = 0.5$. For simplicity we will set the enthalpy of mixing $\epsilon(T) = 0$ for all temperatures. We consider the two-phase equilibrium system consisting of α and β solid phases, with each differing in their lattice parameters. To assist with rapid equilibration, the mobilities were set to be extremely high compared to the pressure relaxation coefficient: $M_A = M_B = 20$, $M_p = 0.1$. In all simulations the cutoff wavelength was set as in Kocher *et al.* [8] to be $\lambda_c = 0.21$.

As a point of clarification, in the following sections we will often refer to processes occurring over a fixed number of "simulation steps," which refer to a scaled physical time rather than the actual numerical time steps due to the adaptive nature of the dynamical time stepping discussed in Sec. III C. The times have all been rounded to the nearest output call.

A. Control of premelted interphase boundaries

When solids containing interfaces or interphase boundaries approach their melting temperature, they have a propensity to undergo a phenomenon known as premelting [29–31]. During this transition, a disordered, metastable liquidlike film forms between the abutting solid phases. With the width of the liquid layer depending on the energetic differences between bulk solid and liquid phases, it thus decreases with decreasing temperature. The formation of the liquid layer is linked to the cost of maintaining the interface or phase boundary energy and its decomposition to distinct solid-liquid interfacial energies. For the case of our eutectic system, below the eutectic, the condition for premelting exists when $\gamma_{\alpha\beta} > \gamma_{\alpha L} + \gamma_{\beta L}$ where γ_{ij} is the surface energy of the interface between phases i and j.

To avoid the growth of either phase this simulation is set up with a system concentration of $\langle c \rangle = 0.5$ such that we have equal phase fractions. The system parameters are the same as those described in the caption of Fig. 3. The misorientation between grains in the bicrystal is initially set to 0.2 rad ≈ 11.459°.

A schematic of the simulation cycle is shown on a constant temperature phase diagram in Fig. 4. While the results of the simulation are shown in Fig. 5, where the average concentration profile over time and a selection of density-concentration visualizations are depicted. The target pressure was initially

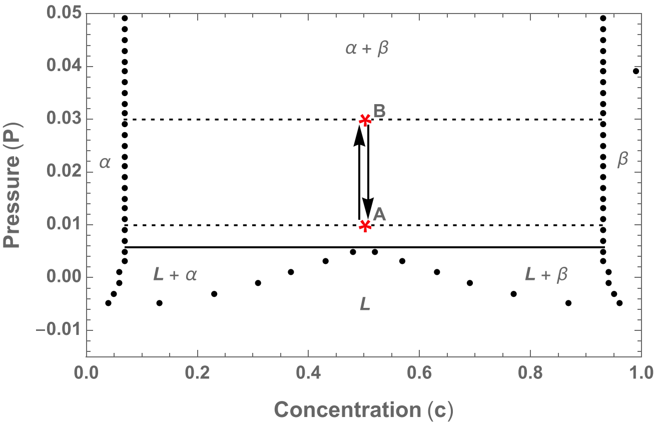

FIG. 4. Schematic view of the simulation cycle demonstrating pressure mediated control of premelted boundary width, with dashed lines showing the expected equilibrium phases of the system at points A and B. The system starts with a pressure and total concentration corresponding to point A. After a period of equilibration the system pressure is quenched to point B. After a further equilibration the system is quenched back to point A.

set to $P_0 = 0.01$ and the system was allowed to equilibrate for 20 000 simulation steps. This initial pressure and temperature combination was chosen such that the system was slightly above the eutectic pressure and would therefore exhibit premelting. The target pressure is then quenched to $P_0 = 0.03$ over 10 000 simulation steps and allowed to equilibrate for a further 10 000 simulations steps. Under this quench we see that the interphase boundary narrows significantly and the amplitude no longer decays to zero between phases. We then quench back to the original pressure of $P_0 = 0.01$ over a further 10 000 simulation steps and allow for a further equilibration of 20 000 simulation steps. Having returned to the initial condition, we see that there is once again an increased level of premelting, however it is reduced compared to the original amount. This is due to a minor change in the crystallographic orientation of the grains, which changes the solid-liquid interfacial and the eventual grain boundary energies.

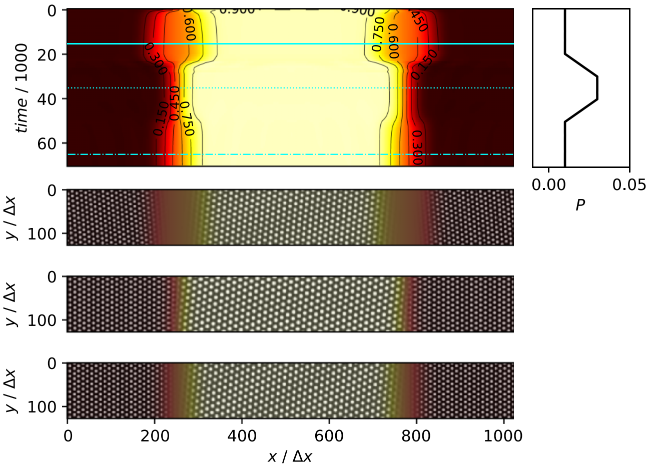

FIG. 5. (Top left) Concentration vs time of the pressure mediated changes to thermodynamic stability. The concentration shown at each time is the concentration value averaged over the short direction of the channel. (Top right) The grand potential density of the system at the time corresponding to the value in the top left. (Upper middle) The density-concentration profile of the system at the $t = 15\,000$ simulation step represented by the solid horizontal line in the top left figure. At this time the pressure is at $P = 0.01$. (Lower middle) The density-concentration profile of the system at $t = 35\,000$ simulation steps represented by the dotted line in the top left figure. At this time the pressure is at $P = 0.03$. (Bottom) The density-concentration profile of the system at $t = 65\,000$ simulation steps represented by the dashed line in the upper left figure. At this time the pressure has once again returned to $P = 0.01$.

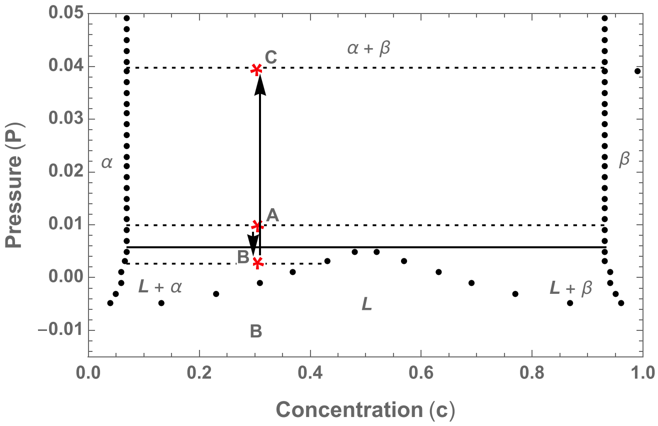

FIG. 6. Schematic view of the simulation cycle demonstrating pressure mediated control of thermodynamic stability, with dashed lines showing the expected equilibrium phases of the system at points A, B, and C. The system starts with a pressure and total concentration corresponding to point A. After a period of equilibration the system pressure is quenched to point B. After a further equilibration in which the beta phase completely melts the system is quenched to point C; over the course of the quench the beta phase nucleates from the solid-liquid front. After the quench is completed the system is once more allowed to equilibrate for some time.

B. Control of thermodynamic stability

While most metallurgical processes of casting are performed at atmospheric pressure conditions [32, p. 287], after casting the treatment of many industrially relevant materials include processes such as annealing and rolling to induce recrystallization and control grain size and distribution [32, Ch. 7]. With the present model we demonstrate that changes to the pressure that a system experiences can affect the stability of its various phases.

To ensure phase elimination we consider a system at $\langle c \rangle = 0.3$, such that there is a preferred fraction of a particular phase. A schematic of the simulation cycle is shown on a constant temperature phase diagram in Fig. 6. Results are observed in Fig. 7, where we show the average concentration profile over time and a selection of density-concentration visualizations. The target pressure is initially set to $P_0 = 0.01$ and the system is allowed to equilibrate for 20 000 simulation steps. The target pressure is then quenched to $P_0 = 0.0025$ over 10 000 simulation steps before being allowed to equilibrate for a

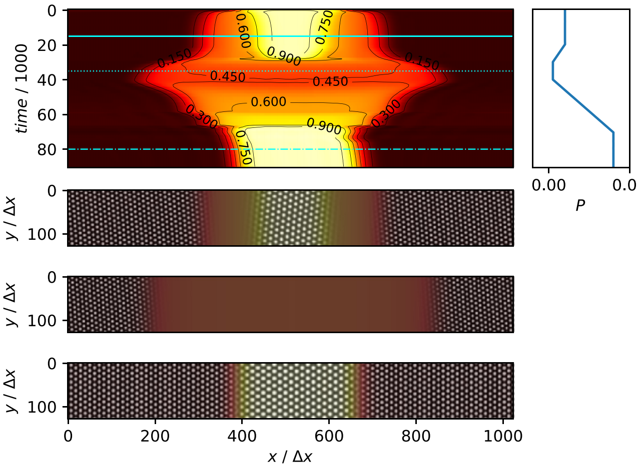

FIG. 7. (Top left) Concentration vs time of the pressure mediated changes to thermodynamic stability. The concentration shown at each time is the concentration value averaged over the short direction of the channel. (Top right) The grand potential density of the system at the time corresponding to the value in the top left figure. (Upper middle) The density-concentration profile of the system at $t = 15\,000$ simulation step, as represented by the solid horizontal line in the top left figure. At this time the pressure is at $P = 0.01$. (Lower middle) The density-concentration profile of the system at $t = 35\,000$ simulation steps as represented by the dotted line in the top left figure. At this time the pressure is at $P = 0.0025$. (Bottom) The density-concentration profile of the system at $t = 80\,000$ simulation steps as represented by the dashed line in the upper left figure. At this time the pressure is at $P = 0.04$.

further 10 000 simulation steps. Over the course of this pressure quench and equilibration, it is evident that both phases undergo melting, however the β phase melts completely due to the quench being below the eutectic pressure. This process is then reversed by a pressure quench to $P_0 = 0.04$ over 30 000 simulation steps. At some point after the simulation has surpassed the original pressure of $P_0 = 0.01$ the system precipitates the β phase from the oversaturated liquid. This hysteresis is due to the metastability of the oversaturated liquid and the fact that this simulation was performed without noise. The eventual precipitation is mediated by the correlation length of the α phase penetrating into the liquid—i.e., the solid phase heterogeneously nucleates from the solid-liquid front.

C. Nonequilibrium interphase boundary motion

In this subsection we demonstrate pressure-induced deviation from the equilibrium phase diagram and the resultant nonequilibrium interphase boundary motion that occurs due to this process. It is noted that as with all structural PFC models, this current model does not presently have an explicit coupling between the pressure or strain of the system and the lattice parameter of the crystal. As such, if the crystal is allowed to relax to its proper lattice parameter at one pressure it will not be able to both maintain its proper lattice parameter and simulation box coherency should the pressure change, barring crystallographic rotations or recrystallization.

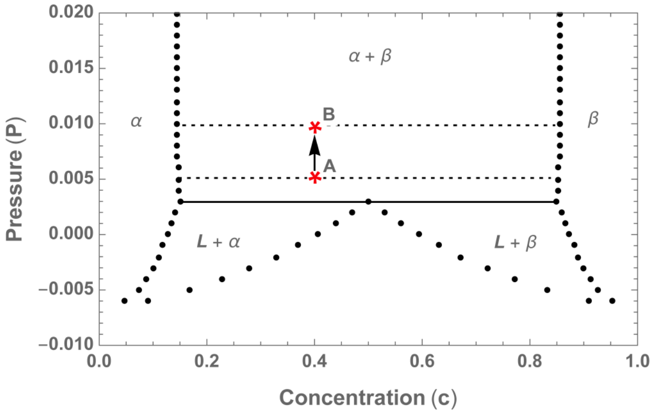

FIG. 8. Schematic view of the simulation cycle demonstrating pressure mediated control of nonequilibrium interphase boundary movement. The system starts with a pressure and total concentration corresponding to point A. After a period of equilibration the system pressure is quenched to point B and allowed to equilibrate. Strain on each phase of the bicrystal will result in nonequilibrium concentrations.

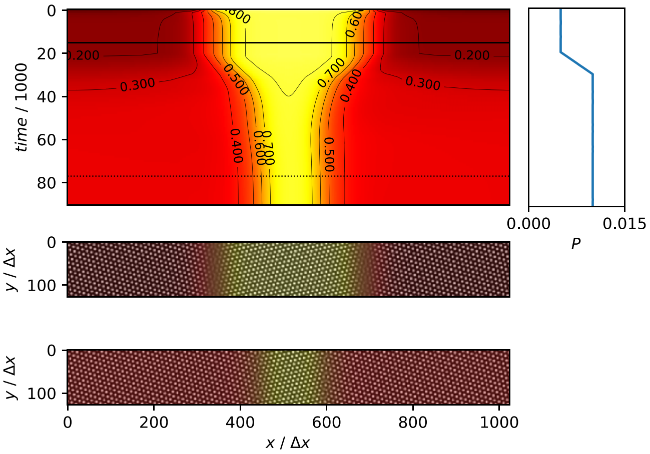

FIG. 9. (Top left) Concentration vs time of the pressure mediated interphase boundary movement. The concentration shown at each time is the concentration value averaged over the short direction of the channel. (Top right) The grand potential density of the system at the time corresponding to the value in the top left figure. (Middle) The density-concentration profile of the system at $t = 15\,000$ simulation step, as represented by the solid horizontal line in the top left figure. At this time the pressure is at $P = 0.005$. (Bottom) The density-concentration profile of the system at $t = 77\,000$ simulation steps as represented by the dotted line in the top left figure. At this time the pressure is at $P = 0.01$.

In the simulations presented in this subsection, we consider an overall system concentration of $\langle c \rangle = 0.4$ and excess free energy parameters $k_{10}^{(A)} = 4\pi/\sqrt{3}$, $\sigma_{10}^{(A)} = 0.8$, $T_M^{(A)} = 1.0$, $k_{10}^{(B)} = 1.1k_{10}^{(A)}$, $\sigma_{10}^{(B)} = 0.8$, and $T_M^{(B)} = 1.0$ such that the increased overlap between peaks will result in larger solubility. A schematic of the simulation cycle is shown on a constant temperature phase diagram in Fig. 8. We show the results of the simulation in Fig. 9, where the average concentration profile over time and a selection of density-concentration visualizations are displayed. The target pressure was initially set to $P_0 = 0.005$ and the system was allowed to equilibrate for 20 000 simulation steps. The target pressure was then quenched to $P_0 = 0.01$ over 10 000 simulation time steps before being allowed to equilibrate for a further 60 000 simulation time steps. The pressure quench and resultant change in volume took the system entirely off equilibrium due to box strain effects. As the α phase in this system has the larger lattice parameter, it is energetically favorable for this phase to take on additional solute, lowering its effective lattice parameter and reducing strain. Due to the limited amount of solute in the system the β phase has two options—lower its volume fraction or lower its concentration. As lowering its concentration would increase its lattice parameter and therefore its strain, the energetically favorable choice is to lower its volume fraction and thus the interphase boundary moves.

VI. STRESS INDUCED GRAIN BOUNDARY MOTION AND SOLUTE DRAG

Control of the growth and coarsening of grains in a solid state material is of particular practical interest due to the intimate relationship between the distribution of grain size and macroscopic material properties [32, Ch. 7]. One of the means by which one can control coarsening is by the addition of various solutes which are attracted to the grain boundaries and have been long known to drag the motion of these boundaries [33,34]. While some work has been done in PFC modeling to study solute drag on moving grain boundaries [12], this work relied on artificial driving forces through ad-hoc impositions of orientation biases.

In this section we illustrate the robustness of our new model and the methodology presented herein to incorporate strain-induced grain boundary motion under isobaric conditions. This will be of use in studies of solute drag and other solid state phenomena to be examined in future work.

Similarly to the simulations discussed in Sec. V, we will consider a binary system where both the solute and solvent prefer a triangular lattice symmetry. For completeness, we added a $k = 0$ mode to the correlation function here in order to control the bulk modulus of our phases and the density jump between them. A depth, $B_x = 1.0$, and width, $\sigma_0 = 0.8$, of the Gaussian controlling the bulk modulus was chosen to be a constant between phases for simplicity; additionally, the depth of this well was chosen to be temperature independent. The correlation kernel with this addition takes the form

$$\tilde{C}_i(k) = -\frac{B_x}{\tau} e^{-\frac{k^2}{2\sigma_0^2}} + e^{-\frac{T}{T_M}} e^{-\frac{(k-k_i)^2}{2\sigma_i^2}}, \tag{36}$$

where for convenience the peak widths have been chosen to have low degrees of overlap. Some care must be taken in selecting either the width of this Gaussian or the cutoff wavelength of the density-smoothing kernel. Should the cutoff wavelength of the smoothing kernel be significantly larger than the width of the $k = 0$ mode of the correlation kernel, oscillatory behavior in concentration can result on wavelengths that are considered long by the smoothing kernel but not penalized by the correlation function. The two-point correlation function of a real material displays a low-k shelf which smoothly transitions to the first peak of the structure. In the XPFC formalism, correlation kernels can have a plateau between this shelf and the first peak—it is this control over parameters that results in this oscillatory behavior for sufficiently poor parameter choices. Thus, reducing the extent of this plateau leads to a reduction of undesirable oscillations in concentration. The phase diagram for this system is shown in Fig. 10 with the thermodynamic parameters discussed in the figure caption.

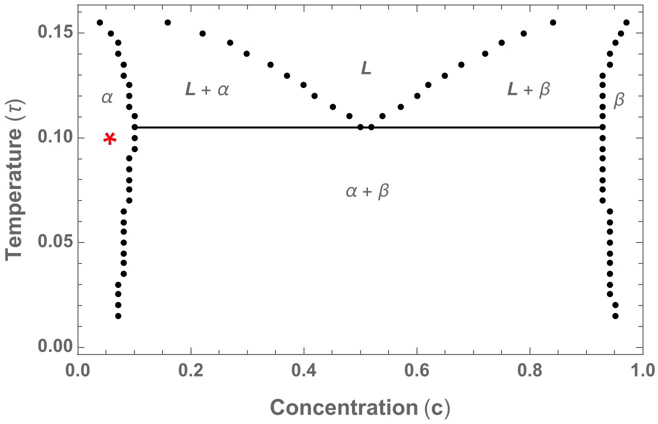

FIG. 10. Phase diagram for the triangle-triangle system with a constant model pressure of $P = 0.05$. The parameters used in the ideal free energy were $t = 1.4$, $v = 1.0$, $w = 0.02$, $c_0 = 0.5$, and $\epsilon(T) = 0$ for simplicity. The correlation kernel for the excess free energy used parameters of $k_{10}^{(A)} = 4\pi/\sqrt{3}$, $\sigma_{10}^{(A)} = 0.6$, $T_M^{(A)} = 1.0$, $k_{10}^{(B)} = 2\pi$, $\sigma_{10}^{(B)} = 0.8$, and $T_M^{(B)} = 1.0$. The $k = 0$ peak which controls the bulk modulus of the system was set to a depth of $B_x = 1.0$ and width of $\sigma_0 = 0.8$ for all phases. The red star denotes the $\langle c \rangle$ and τ values at which the simulation will occurs.

To generate a system with a driving force between two crystals of the same phase, we first generate two supercells for the crystals using a 64×64 pixel grid with rectangular volume element with initial size and constant temperature of $\tau = 0.1$, reference temperatures $T_0 = T_M = 1.0$, and average concentration of $\langle c \rangle = 0.05$ (a generalization of the number conserving feedback loop to a rectangular volume element is discussed in the Appendix). In this case the supercells correspond to two unstressed boxes with a commensurate crystals at orientations of $\theta = 0.0^\circ$ and with initial volume elements $\Delta x(t = 0) = 0.12487858552217967$ and $\Delta y(t = 0) = 0.14419736993450027$ and $\theta \approx 3.67^\circ$, respectively, with respect to the short axis of the eventual channel, with initial volume elements $\Delta x(t = 0) = 0.12099641271809497$ and $\Delta y(t = 0) = 0.13971462290754239$. Just as they do not start equal, the volume elements of the two supercells are not equal post relaxation. Thus, seeding the density profile of one of the supercells into a box with differing dimensions imposes a stress on that crystal. We use this concept to seed the initial condition of the solute drag channel; we set the volume elements of the simulation to that of the relaxed $\theta = 0.0^\circ$ supercell and copy the density profile of the $\theta = 0.0^\circ$ supercell to one part of the simulation domain and the density profile of the $\theta \approx 3.67^\circ$ supercell to the remainder of the

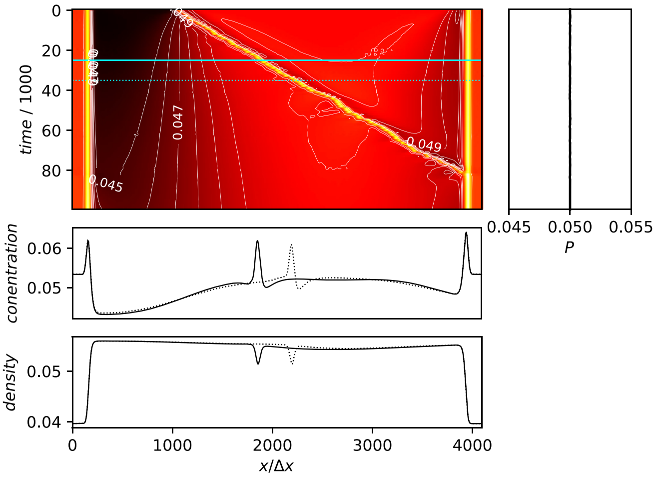

FIG. 11. (Top left) Concentration vs time of the strain induced stress driven grain boundary motion. The concentration shown at each time is the concentration value averaged over the short direction of the channel. (Top right) The grand potential density of the system at the time corresponding to the value in the top left figure. (Middle) The concentration profiles averaged along the short dimension at $t = 25\,000$ and $t = 35\,000$ as represented by the solid and dashed lines in the top left figure, respectively. (Bottom) The total density profiles averaged along the short dimension at $t = 25\,000$ and $t = 35\,000$ as represented by the solid and dashed lines, respectively.

domain. This setup corresponds to an approximate isotropic strain on the box-misaligned crystal of ≈3%.

Once this system has been seeded we allow it to reach as close to an equilibrium as it can achieve without changing the physical structure of the system at any given position. To facilitate this "pseudoequilibration" we run dynamics on the long wavelength components of the free energy using model A dynamics.

$$\frac{\partial(\chi * \rho_i)}{\partial t} \approx -M_i\left(\chi * \frac{\delta F}{\delta \rho_i}\right) \tag{37}$$

Once the pseudoequilibration is complete we simulate the normal conserved dynamics of each density field at a constant system pressure of $P = 0.05$ and density mobilities of $M_A = M_B = 1.0$. To ensure that no crystallographic rotation of the crystal occurs during the simulation we hold the short direction at a constant length, adjusting only the length element in the long direction. Additionally, we reduce the stress in the long direction by utilizing a scheme used by Berry *et al.* [35] and introduce a penalty function to the edges of the system which generates an artificial liquid. The results of this simulation are shown in Fig. 11 and Fig. 12. The unstressed crystal, being more energetically favorable than the stressed crystal, begins to consume the stressed crystal. Solute is attracted to the grain boundary due to its relatively disordered nature, and thus as the grain boundary moves so too must the solute peak. A thorough examination of the individual component mobilities on the speed of the grain boundary motion will be the topic of an upcoming paper.

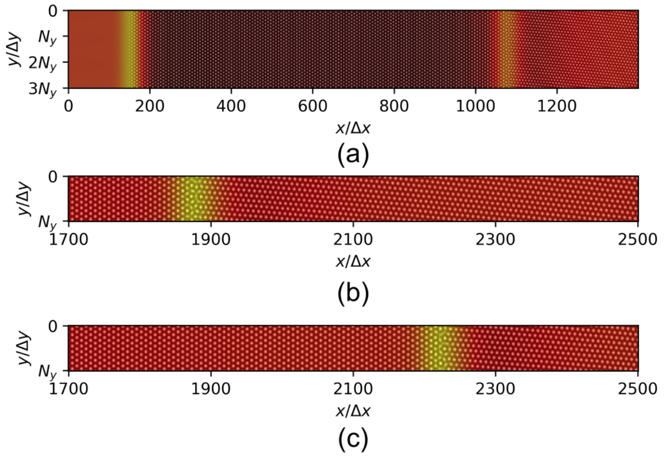

FIG. 12. Density-concentration profiles of the system for some selected subdomain of the system to show various features. (a) The first 1400 pixels in the x direction to demonstrate the liquid penalty layer as well as the system structure at early times, $t = 1000$. The y direction is repeated three times in this figure for ease of visualization. (b) An 800 pixel snapshot at $t = 25\,000$ as represented by the solid line in Fig. 11. (c) The same 800 pixels as (b) but at later time $t = 35\,000$ as represented by the dashed line in Fig. 11.

VII. CONCLUSION

We have presented a relationship that consistently maps the concentration, a long-wavelength field, on to the constituent density fields of a binary alloy, thus making consistent the underlying assumptions used to derive the alloy XPFC model. We have further reformulated XPFC dynamics in terms of the chemical potentials of the individual component densities, thus allowing for proper conserved dynamics in alloys, as well as independent control of the component mobilities. We have presented a more consistent formulation for the control of pressure than previously done, through volume dynamics, and applied these dynamics to an XPFC alloy. We have elucidated the means of generating isobaric phase diagrams and dynamical simulations within the XPFC alloy formalism. We tested the fidelity of dynamical simulations against the corresponding phase diagrams. We also demonstrated the ability to control kinetic processes through changes in pressure, an important avenue for controlling phase transformations not previously available in the PFC literature. Finally we have provided a proof of concept for self-consistently simulating strain induced stress driven grain boundary motion, which could be used for the study of solute drag effects. This work also allows various other strain effects to be considered more consistently as shown in Sec. V C.

ACKNOWLEDGMENTS

We would like to thank Michael Greenwood for helpful discussions on the topic of solute drag. We also thank The National Science and Engineering Research Council (NSERC) of Canada for funding, and Compute Canada for high performance computing resources.

APPENDIX: RECTANGULAR VOLUME ELEMENTS AND ANISOTROPY

Specializing to two dimensions and generalizing to a rectangular volume element Eqs. (24) and (25) become

$$\bar{\rho}(x, y, t + \Delta t) = \bar{\rho}(x, y, t)e^{-\frac{M_p(\bar{\omega}-P_0)}{\Delta x \Delta y}}, \tag{A1}$$

$$J_{\text{isotropic}} = -\sqrt{\Delta x(t)\Delta y(t)} + \sqrt{\Delta x(t_0)\Delta y(t_0)\frac{\int_V d^2r\rho(t)}{\int_v d^2r\rho(t_0)}}. \tag{A2}$$

To further allow for relaxation of any box stresses we also introduce an anisotropic component to the volume flux in the form of an approximated strain energy. Since the ideal contribution should not support any anisotropic stresses we consider only the excess energy when formulating our phenomenology. Thus to crudely measure the change in energy of a given deformation of the system as a whole we propose the phenomenological but qualitative form

$$\epsilon_x = \frac{1}{V}\int_V d^2r\, n(r)\mathcal{F}^{-1}\left\{\frac{\partial \tilde{C}_{\text{nn}}(k)}{\partial k_x}\tilde{n}(k)\right\},$$
$$\epsilon_y = \frac{1}{V}\int_V d^2r\, n(r)\mathcal{F}^{-1}\left\{\frac{\partial \tilde{C}_{\text{nn}}(k)}{\partial k_y}\tilde{n}(k)\right\}, \tag{A3}$$

where $\mathcal{F}^{-1}\{...\}$ denotes the inverse Fourier transform. Such a form has a few attractive features for a single bulk phase; it is agnostic to both the structure of the density field and the box dimensions; it vanishes both in the presence of a liquid and an unstressed crystal; most importantly it is easy to calculate numerically. As we are mostly interested in the stress present in bulk phases, we have explicitly neglected the contribution of gradients in the concentration, under the assumption that they will be negligible far from grain boundaries, interfaces, and explicit defects. Such an assumption is motivated in part by the fact that the grand potential is only strictly analogous to pressure in the absence of interfaces and defects. In this paper we have found generally good results using the grand potential as a stand-in for pressure across various systems with interfaces; we thus assume that an anisotropy motivated by bulk phases can similarly be applied to coexistence.

To apply this anisotropy the guess-check-correct algorithm is slightly modified. The expected change in volume element is calculated with an anisotropic contribution as

$$\delta(\Delta x) \approx \frac{\Delta t M_p}{\Delta x + \Delta y}(\omega - P_0),$$
$$\delta(\Delta y) \approx \frac{\Delta t M_p}{\Delta x + \Delta y}(\omega - P_0) + \frac{\Delta t M_p \Delta x}{\Delta x + \Delta y}(\epsilon_y - \epsilon_x), \tag{A4}$$

where we have chosen to only apply the anisotropy to the y component so as to not double count the isotropic driving due to the crystal elasticity. In this case the time step is scaled based on the larger of the two expected changes to the volume elements. Next the density is adjusted as per Eq. (A1) before changing Δx and Δy as given by Eq. (A4). Finally, Eq. (A2) is applied to both Δx and Δy to ensure proper number conservation.

---

[1] K. R. Elder, N. Provatas, J. Berry, P. Stefanovic, and M. Grant, Phase-field crystal modeling and classical density functional theory of freezing, Phys. Rev. B **75**, 064107 (2007).

[2] K. R. Elder and M. Grant, Modeling elastic and plastic deformations in nonequilibrium processing using phase field crystals, Phys. Rev. E **70**, 051605 (2004).

[3] M. Greenwood, N. Provatas, and J. Rottler, Free Energy Functionals for Efficient Phase Field Crystal Modeling of Structural Phase Transformations, Phys. Rev. Lett. **105**, 045702 (2010).

[4] M. Greenwood, J. Rottler, and N. Provatas, Phase-field-crystal methodology for modeling of structural transformations, Phys. Rev. E **83**, 031601 (2011).

[5] M. Greenwood, N. Ofori-Opoku, J. Rottler, and N. Provatas, Modeling structural transformations in binary alloys with phase field crystals, Phys. Rev. B **84**, 064104 (2011).

[6] N. Smith and N. Provatas, Generalization of the binary structural phase field crystal model, Phys. Rev. Materials **1**, 053407 (2017).

[7] E. J. Schwalbach, J. A. Warren, K.-A. Wu, and P. W. Voorhees, Phase-field crystal model with a vapor phase, Phys. Rev. E **88**, 023306 (2013).

[8] G. Kocher and N. Provatas, New Density Functional Approach for Solid-Liquid-Vapor Transitions in Pure Materials, Phys. Rev. Lett. **114**, 155501 (2015).

[9] N. Wang, N. Smith, and N. Provatas, Investigating gas-phase defect formation in late-stage solidification using a novel phase-field crystal alloy model, Phys. Rev. Materials **1**, 043405 (2017).

[10] K. R. Elder, K. Thornton, and J. J. Hoyt, The kirkendall effect in the phase field crystal model, Philos. Mag. **91**, 151 (2011).

[11] G.-M. Lu, Y.-L. Lu, T.-T. Hu, and Z. Chen, Phase field crystal study on the phase boundary migration induced by the kirkendall effect, Comput. Mater. Sci. **106**, 170 (2015).

[12] M. Greenwood, C. Sinclair, and M. Militzer, Phase field crystal model of solute drag, Acta Mater. **60**, 5752 (2012).

[13] V. Fallah, J. Stolle, N. Ofori-Opoku, S. Esmaeili, and N. Provatas, Phase-field crystal modeling of early stage clustering and precipitation in metal alloys, Phys. Rev. B **86**, 134112 (2012).

[14] V. Fallah, N. Ofori-Opoku, J. Stolle, N. Provatas, and S. Esmaeili, Simulation of early-stage clustering in ternary metal alloys using the phase-field crystal method, Acta Mater. **61**, 3653 (2013).

[15] V. Fallah, A. Korinek, N. Ofori-Opoku, N. Provatas, and S. Esmaeili, Atomistic investigation of clustering phenomenon in the al–cu system: Three-dimensional phase-field crystal simulation and hrtem/hrstem characterization, Acta Mater. **61**, 6372 (2013).

[16] K. R. Elder and Z. F. Huang, A phase field crystal study of epitaxial island formation on nanomembranes, J. Phys.: Condens. Matter **22**, 364103 (2010).

[17] Y. Lu, Y. Peng, and Z. Chen, A binary phase field crystal study for liquid phase heteroepitaxial growth, Superlattices Microstruct. **97**, 132 (2016).

[18] M. Seymour and N. Provatas, Structural phase field crystal approach for modeling graphene and other two-dimensional structures, Phys. Rev. B **93**, 035447 (2016).

[19] E. Alster, K. R. Elder, J. J. Hoyt, and P. W. Voorhees, Phase-field-crystal model for ordered crystals, Phys. Rev. E **95**, 022105 (2017).

[20] Z.-F. Huang, K. R. Elder, and N. Provatas, Phase-field-crystal dynamics for binary systems: Derivation from dynamical density functional theory, amplitude equation formalism, and applications to alloy heterostructures, Phys. Rev. E **82**, 021605 (2010).

[21] J. W. Cahn and J. E. Hilliard, Free energy of a nonuniform system. i. interfacial free energy, J. Chem. Phys. **28**, 258 (1958).

[22] M. Frigo and S. G. Johnson, The design and implementation of fftw3, Proc. IEEE **93**, 216 (2005).

[23] N. Provatas and K. Elder, *Phase-Field Methods in Materials Science and Engineering* (John Wiley & Sons, Berlin, 2011).

[24] L. D. Landau and E. M. Lifshitz, *Statistical Physics, Part 1: Volume 5* (Butterworth-Heinemann, Oxford, 1980).

[25] B. A. Jugdutt, N. Ofori-Opoku, and N. Provatas, Calculating the role of composition in the anisotropy of solid-liquid interface energy using phase-field-crystal theory, Phys. Rev. E **92**, 042405 (2015).

[26] J. G. Kirkwood and E. Monroe, Statistical mechanics of fusion, J. Chem. Phys. **9**, 514 (1941).

[27] T. V. Ramakrishnan and M. Yussouff, First-principles order-parameter theory of freezing, Phys. Rev. B **19**, 2775 (1979).

[28] Wolfram Research, Inc, Mathematica, Version 12.0, Champaign, IL, 2019.

[29] T. E. Hsieh and R. W. Balluffi, Experimental study of grain boundary melting in aluminum, Acta Metall. **37**, 1637 (1989).

[30] A. Adland, A. Karma, R. Spatschek, D. Buta, and M. Asta, Phase-field-crystal study of grain boundary premelting and shearing in bcc iron, Phys. Rev. B **87**, 024110 (2013).

[31] B. B. Straumal, A. Korneva, O. Kogtenkova, L. Kurmanaeva, P. Zieba, A. Wierzbicka-Miernik, S. N. Zhevnenko, and B. Baretzky, Grain boundary wetting and premelting in the cu–co alloys, J. Alloys Compd. **615**, S183 (2014).

[32] W. D. Callister, Jr. and D. G. Rethwisch, *Callister's Materials Science and Engineering* (John Wiley & Sons, New York, 2010).

[33] J. W. Cahn, The impurity-drag effect in grain boundary motion, Acta metallurgica **10**, 789 (1962).

[34] M. Hillert and B. O. Sundman, A treatment of the solute drag on moving grain boundaries and phase interfaces in binary alloys, Acta Metallurgica **24**, 731 (1976).

[35] J. Berry, N. Provatas, J. Rottler, and C. W. Sinclair, Phase field crystal modeling as a unified atomistic approach to defect dynamics, Phys. Rev. B **89**, 214117 (2014).